

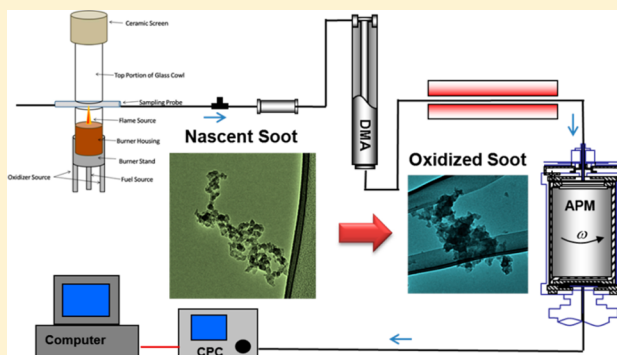
Soot Oxidation Kinetics: A Comparison Study of Two Tandem Ion-Mobility Methods

X. Ma,^{†,‡} C. D. Zangmeister,[‡] and M. R. Zachariah^{†,‡,*}

[†]Department of Mechanical Engineering and Department of Chemistry and Biochemistry, University of Maryland, College Park 20740, Maryland, United States

[‡]National Institute of Standards and Technology, Gaithersburg 20899, Maryland, United States

ABSTRACT: The oxidation kinetics of laboratory-generated soot particles has undergone extensive studies because of its importance in combustion-generated emissions and their control. In this study, we employed and compared two tandem ion-mobility methods, a tandem differential mobility analyzer (TDMA) and a differential mobility analyzer–aerosol particle mass analyzer (DMA–APM), to resolve the oxidation kinetics of soot. Whereas the TDMA method measures changes in particle mobility (i.e., size) from which a mass-based reaction rate can be inferred, the DMA–APM is a direct determination of particle mass change. We monitored the structure evolution of soot during oxidation by determining the mass-mobility scaling exponent of the particle population and found that soot structural changes due to oxidative sintering can perturb and corrupt the apparent reaction kinetics extracted from the TDMA method and suggest that the DMA–APM method probably is a more reliable approach to pursue such measurements. By combining the mass change data from DMA–APM with size change data from TDMA, we obtained the material density and primary particle size of soot aggregates during oxidation. Two reaction regimes were identified with oxidation fully penetrating the particle at low temperatures and partial penetration at high temperatures. The activation energies were determined for the two reaction regimes to be 79 and 201 kJ mol⁻¹, respectively. The results should be useful in designing soot oxidation abatement units.



INTRODUCTION

Soot is produced as an unwanted byproduct from virtually every combustion process from the laboratory burner to diesel engines and power plants. Depending on the source, soot usually has different structure, composition, radiation, and pollutant emission properties. It is the principal component of atmospheric absorbing carbon. When respired, it presents a significant environmental and health hazard due to adsorbed polycyclic aromatic hydrocarbons, which are classified as a known human carcinogen. There is thus considerable interest in abatement of soot by postcombustion-controlled oxidation.

Soot typically consists of many spherical primary particles, which are nearly uniform in size, in an aggregate structure, comprising a broad size distribution within an aerosol population. Experimental evidence suggests that the surface of the particles have a more ordered graphitic layered structure, where the layer planes are aligned parallel to the surface, with a diminishing graphitic order near the particle center.¹

There have been many studies on the oxidation of different types of soot and related materials, such as carbon black, carbon filaments, coal char, and graphite rod, under both noncatalytic and catalytic conditions.² Generally, two temperature ranges are of interest for soot oxidation: high temperature (over 800 °C), as in a flame condition; and low temperature (300–700 °C),

usually found in diesel exhaust systems.² Because of the porous structure of soot primary particles, the nature of soot oxidation is determined by the competition between the rate of surface reaction and the diffusion rate of oxidant into the primary particle core. With this conceptual model in mind, it has been found convenient to consider three regimes:² regime I when the oxidant fully penetrates the solid and the internal surface is reacting, regime II when oxidant penetration is partial and diffusion into the particle is insufficient to supply all of the reactions, and regime III when reaction takes place at the outer surface only.

A variety of techniques have been employed, including thermogravimetric analysis^{3,4} and fixed-bed reactors⁵ for low-temperature studies, shock tube,⁶ and light scattering⁷ within a flame for high-temperature oxidation studies. It is well known that techniques based on bulk samples lead to difficulties in separating diffusion effects from reaction effects, and the polydispersity of the sample may blur the possible size-dependent effects. Previous work in our group using a tandem differential mobility (TDMA) method to study the oxidation of

Received: January 15, 2013

Revised: April 2, 2013

Published: April 12, 2013

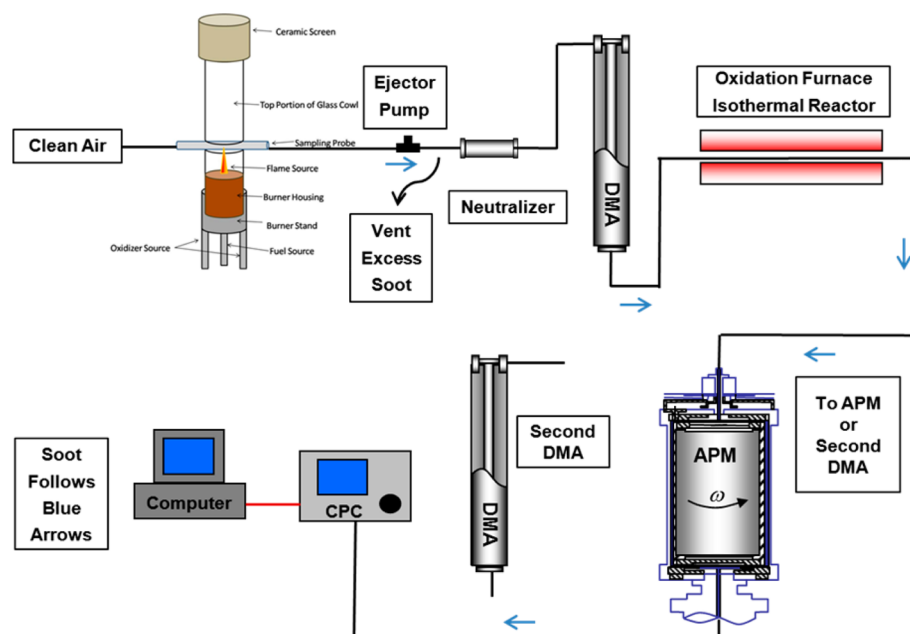


Figure 1. DMA–APM system for measurement of soot oxidation from a diffusion flame source.

freshly generated soot obtained size-dependent reaction kinetics from aerosolized samples, mitigating heat and mass transfer limitations and effects found in studying bulk powder samples.⁸ However, because the TDMA approach is measuring a physical dimension change of the particle, the data analysis requires converting the particle size change to a particle mass change to extract reaction rate. Unfortunately, this conversion from size to mass usually requires an a priori assumption of geometry, which is typically spherical. This spherical assumption is likely in Nienow et al. oxidation kinetics of 30 nm primary soot particles as a function of oxygen partial pressure using the TDMA method.⁹

In this study, we employ a new tandem ion-mobility method (DMA–APM method) to study the size-resolved oxidation kinetics of freshly generated flame soot. The first ion-mobility characterization, DMA size selects soot particles on the basis of a measurement of its equivalent mobility diameter, whereas the second ion-mobility characterization (APM) measures the mass of the particle. The advantage of the DMA–APM method is that it can measure the absolute mass of size-selected (monodispersed) particles independent of particle morphology and material. Thus, the reaction rate can be directly related to particle mass change rate. In this study, the TDMA method is also used to measure the size change of the soot particles under exactly the same conditions. The oxidation kinetics obtained from both methods are compared and discussed.

To monitor the structure change due to oxidation and sintering, we measured the mass-mobility scaling exponent of the soot at different temperatures. By accurately measuring the particle mobility diameter, d_m , and mass, m , over a range of mobility sizes, a power law relationship can be used to extract the mass-mobility scaling exponent, D_m , of the aerosol population:¹⁰

$$m \propto d_p^{D_m} \quad (1)$$

The particle effective density is also an important parameter for the characterization of nonspherical particles and can be

determined by simultaneous measurement of mobility size and particle mass,¹¹

$$\rho_{\text{effective}} = \frac{6m}{\pi d_p^3} \quad (2)$$

whereas the true material density of the soot primary particle has been found to be $\sim 1.8\text{--}2.0 \text{ g cm}^{-3}$,¹² the effective density of soot aggregates is much lower and decreases with particle size.¹³ Furthermore, the effective density also reflects changes in soot fractal structure, which will also be measured in this study.

DMA–APM methods have been widely used in determining the physical properties, such as mass,¹¹ density,¹² porosity,¹⁴ coating growth factor,¹⁵ and mass-mobility scaling exponent,¹⁶ of various environmental particles. However, our study is the first to employ those tandem mobility methods for soot reactivity study.

EXPERIMENTAL SECTION

A schematic of the experimental apparatus is shown in Figure 1. In brief, the experimental system consists of three components: generation of size-selected soot nanoparticles; exposure of soot particles to a controlled oxidative environment; and, finally, measurement of the particle mass (by APM) or size (by a second DMA). For the determination of the aerosol mass-mobility scaling exponent as a function of oxidation temperature, the DMA is placed between the oxidation furnace and the APM.

Soot Generation and Sampling. A Santoro style diffusion burner operating on ethylene fuel was used to generate soot particles.¹⁷ The soot aerosol was sampled from the flame via a sampling method described by Kim et al.¹⁸ An ejector pump was placed downstream of the sampling system providing dilution and creating a low-pressure region in the direction of the aerosol flow with a pressure drop of approximately 1 kPa. The low pressure in the sampling tube draws flow at the flame tip into a 1 mm diameter hole in the sampling probe, which was placed orthogonally to the ethylene diffusion flame. Particle-free, dry dilution air was delivered at 5 LPM through the

sampling probe and mixed with the flame aerosol. To increase the soot particle size, the generated soot was allowed to agglomerate in a 5 L accumulation chamber. The aerosol stream flowed from the accumulation chamber to the ejector pump where additional dilution took place. The final diluted stream was then sampled to create a 1.5 LPM aerosol flow through the rest of the experimental system. The polydispersed soot particles were first sent through a neutralizer to establish a known equilibrium charge distribution and then passed to the first DMA for size selection. For these oxidation studies, we DMA size-selected 100 and 200 nm diameter particles.

Soot Oxidation. Size-selected soot particles were sent to a 30 cm long heated reactor tube with a nominal residence time of about 5 s at an aerosol flow rate of 1.5 LPM at room temperature. Because air was used as the carrier gas, the oxygen concentration in the oxidation furnace is estimated to be 21 vol %. The temperature profile in the quartz tube was measured using a K-type thermocouple.

DMA–APM Mass Measurement. The details of the DMA–APM systems have been discussed previously.^{19–23} In brief, the DMA consists of an annular region between two concentric cylinders with the center cylinder held at high voltage and the outer one at ground. Charged particles of the right polarity feel an attractive force toward the center electrode and move radially inward at an electrophoretic velocity determined by the particle charge and the opposing drag force that is a function of particle size. The force balance between electrical and drag forces implies that at fixed voltage all particles exiting the instrument have (to the resolution of the instrument) equivalent mobility sizes.

The APM consists of two concentric cylindrical electrodes that rotate together at a controlled speed. An electrical field in the annular space is created by applying high voltage on the inner electrode, whereas the outer one is held at ground. Charged particles flowing within the concentric cylinders experience opposing centrifugal and electrostatic forces, and as a result, particles exiting the instrument at fixed voltage and rotation speed all have the same nominal mass. By scanning either the voltage or the rotation speed, the particle mass distribution (independent of particle shape) can be determined. APM mass measurements are independent of particle morphology because the centrifugal force is directly proportional to the mass.

The DMA–APM mass measurement was calibrated with NIST Standard Reference Materials (SRM) PSL spheres of 100.7 nm (SRM 1963A) and 310 nm (SRM 1961). The mass measurement error is within 3.5% for 310 nm PSL and 2.8% for 100.7 nm PSL. Run-to-run error is within 0.2% for 310 nm PSL and 0.14% for 100.7 nm PSL spheres. The DMA–APM method has been successfully used to measure the inherent density²³ and microstructure evolution of nanoparticles,²⁵ evaporation,²³ and hydrolysis²² of zinc nanoparticle, as well as to study the mechanism of aluminum,²⁶ zinc,²¹ and nickel¹⁹ oxidations. Recently, this method was coupled with electrospray particle generation method to quantify directly ligand adsorption to nanoparticles.²⁷

TDMA Particle Size Change Measurement. TDMA experiments were conducted to measure the particle size change resulting from soot oxidation. In a TDMA setup, DMA1 is used to size select particles, and DMA2 is used to measure the size change of the monodispersed particles resulting from a physical or chemical transformation. In our experiment, DMA1 and DMA2 were operated at a sheath flow rate of 10 LPM and

aerosol flow of 1.5 LPM. On the basis of the transfer function of DMA, we estimate an uncertainty of 4% in the peak particle size. DMA1 was set at a certain voltage, and DMA2 was operated at scanning mode. Measurements bypassing the oxidation furnace were used to correct for any slight offset between DMA1 and DMA2.

Mass-Mobility Exponent Measurement. Because soot aggregates are clearly nonspherical, we first determine the relationship between the particle mobility and its mass. To determine the mass-mobility scaling exponent of the soot population, the masses of different sizes of soot particles were measured. On the basis of the particle size distribution, 7 different particle sizes were selected from 50 to 200 nm at an increment of 25 nm. The particle mass was plotted against the particle size and fit to yield a power law relationship from which the mass-mobility scaling exponent was extracted (eq 1). For our experiments, the mass-mobility scaling exponent was measured for soot oxidized at different temperatures.

TEM Sample Collection and Analysis. Samples for electron-microscopic analysis were collected exiting the tube furnace by electrostatically precipitating the aerosol onto a TEM grid (200 mesh copper grids coated with lacey carbon film). The transmission electron microscope (JEOL 2100) was operated at an accelerating voltage of 100 kV to obtain images of particles deposited at different conditions. High-resolution TEM images were also taken to determine the primary particle size.

RESULTS AND DISCUSSION

The nascent soot particles generated from the burner and sampled after the accumulation chamber, as shown in parts a and c of Figure 2, are fractal-like aggregates with a primary particle size of about 17 ± 2 nm. The DMA-based aerosol size distribution shows a monomodal distribution with a peak size around 125 nm. The mass-mobility scaling exponent of the

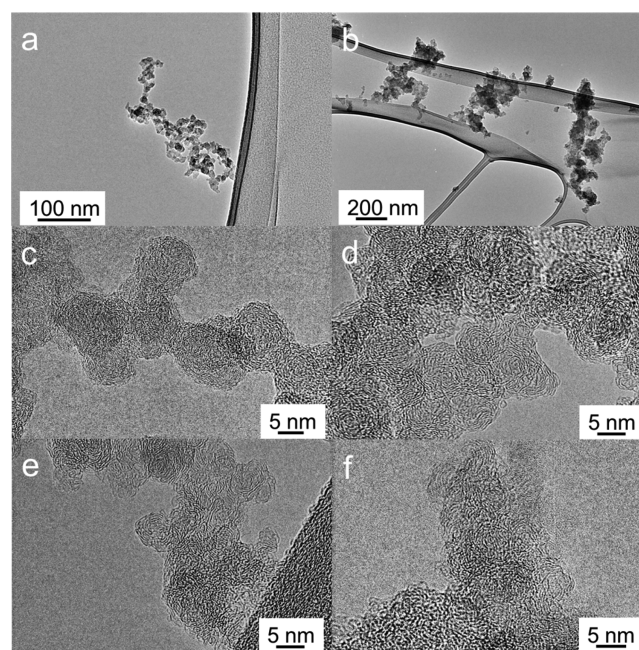


Figure 2. TEM images of (a) soot aggregate at room temperature, (b) soot aggregates oxidized at 900 °C, (c) high-resolution TEM image of soot at room temperature, (d) 700 °C, (e) 800 °C, (f) 900 °C.

fresh soot aerosol was determined by the DMA–APM method to be 2.24 (room temperature data in Figure 3). The abscissa in

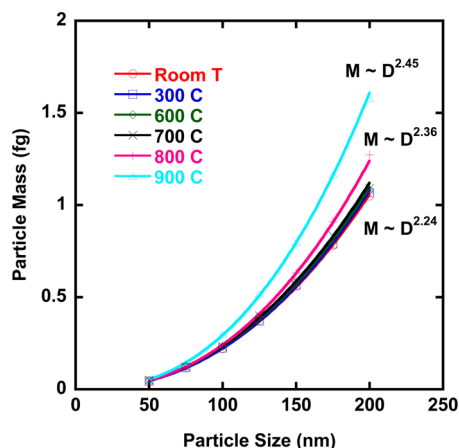


Figure 3. Mass-mobility exponent measurements at different temperatures.

Figure 3 is the mobility size after the first DMA selection. Considering the relationship between mobility size and radius of gyration of particles, the mass mobility scaling exponent value 2.24 corresponds to a fractal dimension of 1.78 for diffusion limited aggregates.²⁸

The particle mass as a function of oxidation temperature is shown in Figure 4 for a 100 nm mobility diameter particle. The

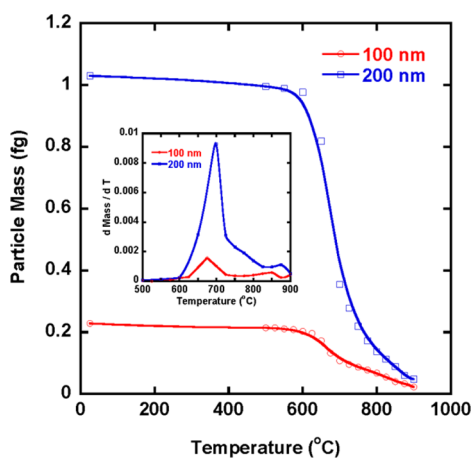


Figure 4. Particle mass vs temperature for 100 and 200 nm soot.

results show that particle mass decreases slightly from room temperature to 600 °C, which probably can be attributed to the evaporation of volatile organics adsorbed on the particle surface. The major decrease in particle mass occurs between 600 and 725 °C. This rapid mass change regime we refer to as low-temperature soot oxidation. From 725 °C up to 900 °C, the oxidation transitions to what we refer to as the high-temperature reaction regime, with a less steeped slope in the particle mass plot. The different oxidation regimes can be clearly observed from the differential mass plot as shown in the inset of Figure 4. At 900 °C, the particle mass decreased to less than 10% of the initial particle mass, which is approaching the mass measurement limit of the instrument.

We now turn to a comparison of what the TDMA measurement shows under the same conditions. The results

of TDMA particle size change and DMA–APM mass change for size-selected 100 nm soot particles are presented in Figure 5. These results show that both particle size and particle mass

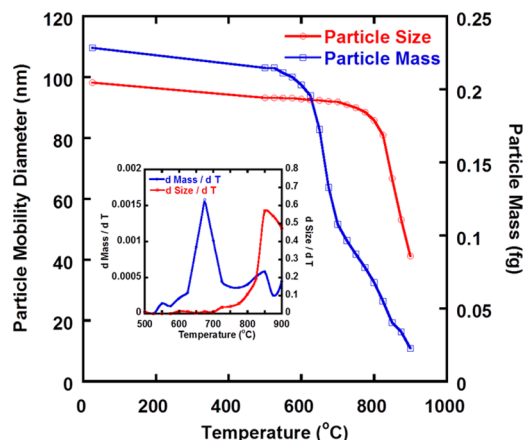


Figure 5. Comparison of TDMA (left axis) and DMA–APM (right axis) results for oxidation of 100 nm soot particle.

decrease slightly from room temperature to 500 °C. However, it is evident from the plot that the apparent onset temperature of oxidation is different for the two methods under the same oxidation conditions. At low temperatures, about a 50% mass change was observed with DMA–APM between 600 and 700 °C. In contrast, the TDMA method only shows a few percent decrease in size. At high temperatures, the TDMA shows more than a 50% change in particle size between 800 and 900 °C, whereas DMA–APM mass measurement only exhibits a 20% change in mass loss in the same temperature regime. The TDMA data shows a fast particle size change regime occurring above 800 °C, which is consistent with our previous work,⁸ but failed to show any apparent oxidation in the low-temperature oxidation regime.

To resolve the differences between these two tandem ion-mobility methods, the mass-mobility scaling exponent was measured at various temperatures to enable a more direct mass-based comparison between the two methods as well as to characterize any structural change during oxidation. The result is shown in Figure 3. The abscissa in Figure 3 is the mobility size after DMA selection, and the ordinate is the measured mass after thermal treatment. The mass-mobility scaling exponent is essentially constant at 2.24 from room temperature up to 700 °C, which indicates no structure change occurs during this oxidation stage. We envision that the soot aggregate loses mass uniformly from each primary particle while maintaining the same relative geometry among the primaries. The mass-mobility scaling exponent changed to 2.36 at 800 °C and further increased to 2.45 at 900 °C, which implies some structure compaction of the soot aggregate. This structure change, which is most probably due to the oxidative sintering at high temperatures, is confirmed by the TEM image shown in part d of Figure 2 for soot aggregates oxidized at 900 °C. High-resolution TEM images presented in parts d–f of Figure 2 clearly show the fusing and overlapping of primary particles with increasing temperature. Thus, under these thermal and oxidative conditions, the changes in size as measured by the TDMA are contributions from both particle size decrease due to oxidation and aggregate structure collapse.

The soot effective density as a function of particle size for various oxidation temperatures is shown in Figure 6. The

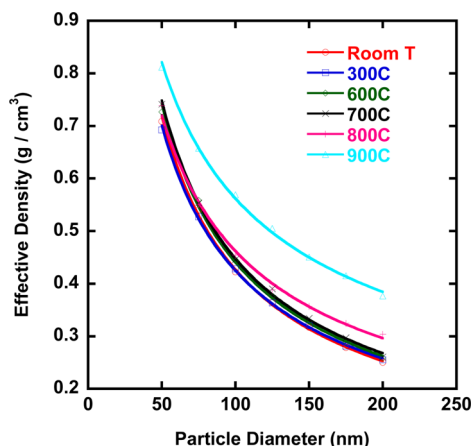


Figure 6. Effective density of soot as a function of particle size for different oxidation temperatures.

effective density is observed to decrease monotonically with particle size and with some temperature dependence. For our studies, we observe the highest effective density for 50 nm soot at 900 °C of 0.81 g cm⁻³ and a lowest value of 0.25 g cm⁻³ for room temperature 200 nm soot particles. Those results are comparable with previous measurements.^{13,16} Analogous to the mass-mobility relationship in Figure 3, the effective density can be described by a power law function. The effective density curves essentially overlap with each other up to 700 °C, indicating a similarity in the aggregate structure as expected but shows an increase in density at 800 °C and higher, which is consistent with particle structure compaction. As might be expected, the largest changes with temperature occurs for the largest aggregates.

A change in structure, however, will not explain why at low temperature the mass is decreasing while the mobility size is essentially constant. We should at this point keep in mind that the TDMA measurement is an external drag force measurement; thus, all mobility changes are inferred as being due to oxidation occurring on the surface of the particle. However, previous experimental data has suggested that significant oxygen penetration into the particle occurs at low temperatures.⁴ In this case, one should expect that, at low temperatures where the chemistry is slow, diffusive penetration of oxygen within the interior of the particle results in oxidative chemistry on both the surface and within the particle, while at high temperatures, the increased reaction rate will promote surface chemistry at the expense of the diffusive transport of oxygen to the interior of the particle. Reaction within the particle will necessarily decrease the absolute particle density. Furthermore, our observed small mobility size change and large mass change between 600 to 725 °C is consistent with a decrease in material density.

Since the mass of a soot aggregate, m , is

$$m = \frac{\pi N \rho d^3}{6} \quad (3)$$

where N is the number of number of primary particles in an aggregate, ρ is the material density of soot primary particles, and d is the primary particle size. Because the mass-mobility scaling exponent measurement suggests no structure change up

to 700 °C, we can reasonably assume that, during low-temperature oxidation, the number of primary particles within an aggregate is conserved. If we further assume the well-known relationship for the mobility diameter of an aggregate in the slip regime formed under diffusion limited aggregation,²⁸

$$d_m = dN^{0.46} \quad (4)$$

we can for 100 nm soot aggregates calculate N to be ~ 47 primaries. On the basis of the particle mass from APM, and size change from TDMA, we use eqs 3 and 4 to extract the soot material density and the primary particle size at room temperature and between 600 to 700 °C.

The results are displayed in Table 1 and show the material density of soot decreased from 1.99 g/cm³ at room temperature

Table 1. Density and Primary Particle Size of 100 nm Soot Aggregates after Oxidation in the Low-Temperature Regime Using TDMA–APM Results

temperature (°C)	material density (g/cm ³)	primary particle diam
25	1.99	16.7
600	2.09	15.8
625	2.05	15.7
650	1.81	15.7
675	1.40	15.7
700	1.15	15.6

by about 42% to 1.15 g/cm³ at 700 °C. We also observed a slight material density increase between 600 and 625 °C, which is consistent with the evaporation of low density volatile organics. Our data suggest a more porous internal structure of soot primaries evolves during the oxidation. The small change in primary particle diameter is consistent with the small change in aggregate mobility size.

At high oxidation temperatures (above 800 °C), sintering effects will decrease the number of primaries, and thus, eqs 2 and 3 are no longer valid.

Because the TDMA fails to detect porous reactions at low temperature and there are coupled effects of sintering and oxidation at high temperatures, we will limit our subsequent analysis of the high-temperature regime to the DMA–APM measurements to extract oxidation kinetics for both temperature regimes. The rate of a solid-state reaction can be generally described by

$$\frac{da}{dt} = Ae^{-(E_a/RT)} f(a) \quad (5)$$

where A is the prefactor, E_a is the activation energy, T is absolute temperature, R is the gas constant, a is the extent of conversion, and $f(a)$ is the reaction model. At low temperatures, because diffusion is fast enough to penetrate the soot surface (as evidenced by a drop in material density), the oxidation process can be considered reaction-rate-limited. Previous experimental work at low temperatures^{4,5,29} has shown that soot oxidation is a first-order process; thus, a first-order reaction model³⁰ ($g(a) = -\ln(1 - a)$) is used to fit the low-temperature kinetics data. Here, $g(a) = \int_0^a (d\alpha/f(\alpha))$ is the integral form of $f(\alpha)$. At high temperatures, the reaction only partially penetrates the particle (diffusion-controlled); thus, we employ a 3D-diffusion model³⁰ ($g(\alpha) = (1 - (1 - \alpha)^{1/3})^2$) to fit the kinetics. Using the mass change results from the DMA–APM, the resulting reaction rate constants are plotted in Arrhenius form and shown in Figure 7. Two reaction

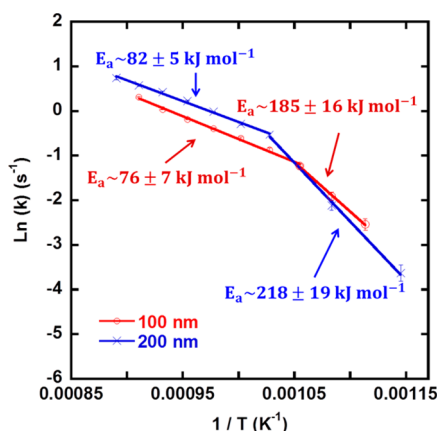


Figure 7. Arrhenius plot of reaction rate for 100 and 200 nm soot oxidation.

regimes can be clearly distinguished from the Arrhenius plot. The oxidation activation energies for 100 nm soot are 185 ± 16 and 76 ± 7 kJ mol^{-1} for low- and high-temperature regimes, respectively. For the 200 nm soot, we obtain 218 ± 19 and 82 ± 5 kJ mol^{-1} for the low- and high-temperature regimes, respectively. Basically, the activation energies for 100 and 200 nm soot show similar values, which are to be expected because the soot aggregates are made up of primary particles of the same size. Taking the average of the activation energies obtained for 100 and 200 nm soot, we obtain activation energies of ~ 200 kJ mol^{-1} in the low-temperature regime and ~ 80 kJ mol^{-1} in the high-temperature regime. One interesting observation is that the 200 nm soot has a slightly higher reaction rate constant than 100 nm soot at the high-temperature regime. The reader is reminded that at high temperatures, the soot structure becomes more compact due to sintering. The higher reaction rate of 200 nm soot particles may suggest that they are not as sintered as 100 nm soot and, therefore, have higher specific surface area available for reaction.

The activation energies observed by others in the low-temperature oxidation regime are found to cover a wide range, between 102 and 210 kJ mol^{-1} , and reflect the wide variety of soot sources and characterization methods.² Our measured activation energy values fall into this range. However, there are few data available for high-temperature oxidation. It is well known that, for the combustion of porous carbon particles, with increasing temperature, there is a transition from regime I to regime II (from reaction-controlled to diffusion-controlled).^{31,32} It has also been shown that the reaction rate in the diffusion-controlled zone (regime II) is proportional to the square root of the rate constant.³³ Because the intrinsic reaction activation energy is related to the reaction rate constant through the Arrhenius equation, the apparent activation energy for the reaction should be 1/2 the intrinsic activation energy of the reaction. Our observations are consistent with a transition from reaction to diffusion control ~ 675 $^{\circ}\text{C}$ based on a drop in the activation energy by slightly over a factor of 2. The results should be useful to those interested in designing soot oxidation abatement units that can be retrofitted to diesel or other internal combustion engines process streams.

CONCLUSIONS

In summary, soot oxidation kinetics was studied using two tandem ion-mobility methods (TDMA and DMA-APM). The TDMA method measures the particle mobility size change

resulting from oxidation, whereas the DMA-APM method directly determines the mass change due to oxidation. We found a change in soot structure change due to oxidative sintering by measuring the mass-mobility scaling exponent. This structure change leads to a higher apparent oxidation rate as measured by TDMA method and suggests that the DMA-APM method probably is a more reliable approach. By combining the size change data and the mass change data, we identified two reaction regimes for soot oxidation. The low-temperature regime below ~ 700 $^{\circ}\text{C}$ with an activation energy of 201 kJ mol^{-1} corresponds to a reaction control with oxidation occurring within the particle and a mass-transfer-controlled regime at higher temperature with an activation energy 79 kJ mol^{-1} . Our observed reaction kinetics are consistent with the combustion of porous solid carbon particles.

AUTHOR INFORMATION

Corresponding Author

*E-mail: mrz@umd.edu.

Notes

The authors declare no competing financial interest.

REFERENCES

- (1) Donnet, J.-B.; Bansal, R. C.; Wang, M.-J. *Carbon Black Science and Technology*; Marcel Dekker, Inc.: New York, 1993.
- (2) Stanmore, B. R.; Brilhac, J. F.; Gilot, P. The Oxidation of Soot: A Review of Experiments, Mechanisms and Models. *Carbon* **2001**, *39*, 2247–2268.
- (3) Stratakis, G. A.; Stamatelos, A. M. Thermogravimetric Analysis of Soot Emitted by a Modern Diesel Engine Run on Catalyst-Doped Fuel. *Combust. Flame* **2003**, *132*, 157–169.
- (4) Gilot, P.; Bonnefoy, F.; Marcuccilli, F.; Prado, G. Determination of Kinetics Data for Soot Oxidation – Modeling of Competition Between Oxygen Diffusion and Reaction During Thermogravimetric Analysis. *Combust. Flame* **1993**, *95*, 87–100.
- (5) Neeft, J. P. A.; Nijhuis, T. X.; Smakman, E.; Makkee, M.; Moulijn, J. A. Kinetics of the Oxidation of Diesel Soot. *Fuel* **1997**, *76*, 1129–1136.
- (6) Park, C.; Appleton, J. P. Shock – Tube Measurements of Soot Oxidation. *Combust. Flame* **1973**, *20*, 369–379.
- (7) Puri, R.; Richardson, T. F.; Santoro, R. J.; Dobbins, R. A. Aerosol Dynamic Process of Soot Aggregates in a Laminar Ethene Diffusion Flame. *Combust. Flame* **1993**, *92*, 320–333.
- (8) Higgins, K. J.; Jung, H. J.; Kittelson, D. B.; Roberts, J. T.; Zachariah, M. R. Size-Selected Nanoparticle Chemistry: Kinetics of Soot Oxidation. *J. Phys. Chem. A* **2002**, *106*, 96–103.
- (9) Nienow, A. M.; Roberts, J. T.; Zachariah, M. R. Surface Chemistry of Nanometer-Sized Aerosol Particles: Reactions of Molecular Oxygen with 30 nm Soot Particles as a Function of Oxygen Partial Pressure. *J. Phys. Chem. B* **2005**, *109*, 5561–5568.
- (10) Park, K.; Kittelson, D. B.; McMurry, P. H. Structural Properties of Diesel Exhaust Particles Measured by Transmission Electron Microscopy (TEM): Relationships to Particle Mass and Mobility. *Aerosol Sci. Technol.* **2004**, *38*, 881–889.
- (11) McMurry, P. H.; Wang, X.; Park, K.; Ehara, K. The Relationship between Mass and Mobility for Atmospheric Particles: A New Technique for Measuring Particle Density. *Aerosol Sci. Technol.* **2002**, *36*, 227–238.
- (12) Park, K.; Kittelson, D. B.; Zachariah, M. R.; McMurry, P. H. Measurement of Inherent Material Density of Nanoparticle Agglomerates. *J. Nanopart. Res.* **2004**, *6*, 267–272.
- (13) Maricq, M. M.; Ning, X. The Effective Density and Fractal Dimension of Soot Particles from Premixed Flames and Motor Vehicle Exhaust. *J. Aerosol Sci.* **2004**, *35*, 1251–1274.
- (14) Lee, S. Y.; Chang, H.; Ogi, T.; Iskandar, F.; Okuyama, K. Measuring the Effective Density, Porosity, and Refractive Index of

Carbonaceous Particles by Tandem Aerosol Techniques. *Carbon* **2011**, *49*, 2163–2172.

(15) Xue, H.; Khalizov, A. F.; Wang, L.; Zheng, J.; Zhang, R. Effects of Coating of Dicarboxylic Acids on the Mass-Mobility Relationship of Soot Particles. *Environ. Sci. Technol.* **2009**, *43*, 2787–2792.

(16) Park, K.; Cao, F.; Kittelson, D. B.; McMurry, P. H. Relationship between Particle Mass and Mobility for Diesel Exhaust Particles. *Environ. Sci. Technol.* **2003**, *37*, 577–583.

(17) Bueno, P. A.; Havey, D. K.; Mulholland, G. W.; Hodges, J. T.; Gillis, K. A.; Dickerson, R. R.; Zachariah, M. R. Photoacoustic Measurements of Amplification of the Absorption Cross Section for Coated Soot Aerosols. *Aerosol Sci. Technol.* **2011**, *45*, 1217–1230.

(18) Kim, S. H.; Fletcher, R. A.; Zachariah, M. R. Understanding the Difference in Oxidative Properties between Flame and Diesel Soot Nanoparticles: The Role of Metals. *Environ. Sci. Technol.* **2005**, *39*, 4021–4026.

(19) Zhou, L.; Rai, A.; Piekiet, N.; Ma, X. F.; Zachariah, M. R. Ion-Mobility Spectrometry of Nickel Nanoparticle Oxidation Kinetics: Application to Energetic Materials. *J. Phys. Chem. C* **2008**, *112*, 16209–16218.

(20) Ma, X. F.; Zachariah, M. R.; Zangmeister, C. D. Crumpled Nanopaper from Graphene Oxide. *Nano Lett.* **2012**, *12*, 486–489.

(21) Ma, X. F.; Zachariah, M. R. Oxidation Anisotropy and Size-Dependent Reaction Kinetics of Zinc Nanocrystals. *J. Phys. Chem. C* **2009**, *113*, 14644–14650.

(22) Ma, X.; Zachariah, M. R. Size-Resolved Kinetics of Zn Nanocrystal Hydrolysis for Hydrogen Generation. *Int. J. Hydrogen Energy* **2010**, *35*, 2268–2277.

(23) Ma, X.; Lall, A. A.; Mulholland, G. W.; Zachariah, M. R. Evaporation Anisotropy of Free Nanocrystals. *J. Phys. Chem. C* **2011**, *115*, 16941–16946.

(24) Kim, S. H.; Mulholland, G. W.; Zachariah, M. R. Density Measurement of Size Selected Multiwalled Carbon Nanotubes by Mobility-Mass Characterization. *Carbon* **2009**, *47*, 1297–1302.

(25) Liu, Q.; Ma, X.; Zachariah, M. R. Combined On-Line Differential Mobility and Particle Mass Analysis for Determination of Size Resolved Particle Density and Microstructure Evolution. *Microporous Mesoporous Mater.* **2012**, *153*, 210–216.

(26) Rai, A.; Park, K.; Zhou, L.; Zachariah, M. R. Understanding the Mechanism of Aluminium Nanoparticle Oxidation. *Combust. Theory Modell.* **2006**, *10*, 843–859.

(27) Guha, S.; Ma, X.; Tarlov, M. J.; Zachariah, M. R. Quantifying Ligand Adsorption to Nanoparticles Using Tandem Differential Mobility Mass Analysis. *Anal. Chem.* **2012**, *84*, 6308–6311.

(28) Sorensen, C. M. The Mobility of Fractal Aggregates: A Review. *Aerosol Sci. Technol.* **2011**, *45*, 765–779.

(29) Brilhac, J. F.; Bensouda, F.; Gilot, P.; Brillard, A.; Stanmore, B. Experimental and Theoretical Study of Oxygen Diffusion within Packed Beds of Carbon Black. *Carbon* **2000**, *38*, 1011–1019.

(30) Khawam, A.; Flanagan, D. R. Solid-State Kinetic Models: Basics and Mathematical Fundamentals. *J. Phys. Chem. B* **2006**, *110*, 17315–17328.

(31) Essenhigh, R. H.; Klimesh, H. E.; Fortsch, D. Combustion Characteristics of Carbon: Dependence of the Zone I-Zone II Transition Temperature (T-c) on Particle Radius. *Energy Fuels* **1999**, *13*, 826–831.

(32) Essenhigh, R. H.; Fortsch, D.; Klimesh, H. E. Combustion characteristics of carbon: Influence of the Zone I-Zone II transition on burn-out in pulverized coal flames. *Energy Fuels* **1999**, *13*, 955–960.

(33) Walker, P. L.; Rusinko, F.; Austin, L. G. Gas Reactions of Carbon. *Adv. Catal.* **1959**, *11*.